



RESEARCH ARTICLE OPEN ACCESS

Techno-Economic Assessment of Manufacturing Membrane Electrode Assemblies for PEM Fuel Cells: Focus on Coating Technologies

Jakob Hog  | Diego Matali Goya | Julius Wild | Linda Ney  | Nada Zamel

Fraunhofer Institute for Solar Energy Systems, Freiburg, Germany

Correspondence: Jakob Hog (jakob.hog@ise.fraunhofer.de)

Received: 18 November 2025 | **Revised:** 21 January 2026 | **Accepted:** 10 February 2026

Keywords: MEA production | PEM fuel cell | Pt-loading | rotary screen printing | slot-die coating | techno-economic assessment

ABSTRACT

High manufacturing costs of proton exchange membrane (PEM) fuel cells remain a significant obstacle to their widespread adoption in transportation applications. To address this, roll-to-roll (R2R) processes are proposed to increase production throughput and reduce membrane electrode assembly (MEA) costs. Among R2R-compatible coating processes, slot-die coating (SDC) represents the state-of-the-art technology, while rotary screen printing (RSP) offers advantages in structured and intermittent printing, providing additional design freedom for catalyst layers (CL). This study examines the cost implications of both coating processes for a specific set of R2R machines to be implemented at Fraunhofer ISE. Technical boundary conditions and operational limitations are evaluated and integrated into a comprehensive continuous process cost of ownership model capturing expenses throughout the production chain, from catalyst ink raw materials to the final seven-layer MEA. A methodology is presented for determining consumable costs at various purchasing volumes, combining literature values with supplier quotations. By integrating performance data from experimentally produced MEAs with the cost model, an approach is developed to determine optimum platinum (Pt) loadings for cost per kW for given materials. The identified optimal Pt loadings of 0.44–0.54 mg_{Pt} cm⁻² demonstrate that the cell performance is crucial for further cost reductions of fuel cells.

1 | Introduction

It is widely acknowledged that increasing the manufacturing volume reduces the cost of a final product [1]. However, the critical question centers on identifying precisely where these cost savings emerge within the manufacturing process chain and what insights can be derived to further optimize the product design. For proton exchange membrane fuel cells (PEMFCs), this understanding is particularly valuable since the membrane electrode assembly (MEA) remains one of the dominant cost drivers in a complete stack [2].

While large-scale deployment remains limited by high costs, low-temperature PEMFC are widely recognized as a key low-

emission technology for decarbonizing the transport sector, which accounts for approximately 20% of global CO₂ emissions [3, 4]. Special focus is placed on PEMFCs for heavy-duty vehicles, as in Europe they contribute a disproportionate 23% of transport emissions while representing only 2% of all vehicles [5, 6].

Despite achieving technical maturity at laboratory scale, the large-scale market penetration of PEMFCs continues to face economic and production-related challenges [7, 8]. The MEA represents the core component and requires costly as well as specialized materials like platinum-based inks and perfluorosulfonic acid membranes. These inks are processed into catalyst layers (CL) using various coating and printing techniques such as slot-die coating (SDC), spray coating, inkjet printing, gravure

This is an open access article under the terms of the [Creative Commons Attribution](https://creativecommons.org/licenses/by/4.0/) License, which permits use, distribution and reproduction in any medium, provided the original work is properly cited.

© 2026 The Author(s). *Fuel Cells* published by Wiley-VCH GmbH.

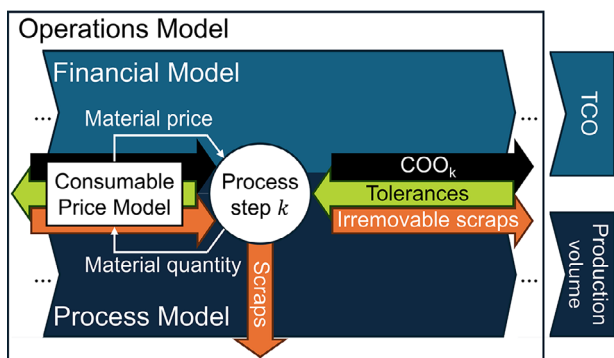


FIGURE 1 | Conceptual structure of the continuous process cost of ownership (CPCO) model for a single process step k . The framework integrates the operations model, financial model, and process model of process-based cost modeling to calculate step-level cost of ownership (COO) [21, 23].

printing and screen printing [9–13]. The objective is to achieve high throughput while maintaining reliability and homogeneity of the printed CL [14]. Given the substantial capital expenditure required for such equipment, a robust techno-economic assessment is essential before making investment decisions [15].

Numerous investigations have explored the economics of PEMFCs from various perspectives. Studies by James et al. and Wei et al. provide in-depth insights into the cost structure of PEMFC materials and stack components, establishing valuable benchmarks [16, 17]. These works employ design for manufacturing and assembly (DFMA) to estimate the value chain from raw materials to the complete PEMFC system, while Marocco et al. utilize the DFMA approach to investigate the system cost of a PEMFC backup power generator, incorporating learning curve assumptions for consumable pricing [18]. Gebert introduced a methodology focused on statistical evaluations of price distributions and demonstrated its application for bipolar plates and various membrane ionomers [19]. In addition, process-based cost modeling (PBCM) has been employed by Kampker et al. to estimate the PEMFC system cost at various production scales, though with limited detail on the consumable cost structure and equipment specifications [20].

While these studies provide comprehensive value chain perspectives spanning from consumables to complete systems, an opportunity exists to examine how specific machinery design features and operational parameters influence production economics. This paper addresses this opportunity by adopting the perspective of an MEA producer operating specific machinery to investigate the relationship between throughput, equipment characteristics, and resulting product costs, focusing on the value chain from consumables to the MEA only. This is achieved by combining the SEMI-E35 Cost of Ownership methodology with extensions proposed by Nold, adapting the total cost of ownership (TCO) framework to roll-to-roll (R2R) MEA production [21, 22]. Combined with a detailed breakdown of the consumables and their cost evolution across different production volumes, this forms the basis for the cost calculation. The TCO approach is adapted for R2R processing due to its inherent focus on machinery and process execution capabilities. However, when determining unit manufacturing costs, this framework can be

reinterpreted as the process-centric PBCM or product-centric DFMA methodologies as shown in the following section [23–25].

Applied to the MEA production, the model encompasses every major manufacturing step, from ink mixing to final MEA assembly. Two representative scenarios are analyzed to quantify how technical and operational constraints govern achievable throughput, complemented by statistical evaluation. Experimental performance data from in-house produced MEAs are utilized to convert the calculated areal cost to cost per kW. In contrast to previous literature that uses predetermined platinum (Pt) loadings that balance performance, durability, and cost [24], this work extends the framework to determine the optimal Pt-loading to minimize the cost per kW for a given scenario.

2 | Materials and Methods

The goal of this work is to estimate the cost of a manufacturer producing MEAs based on consumable and equipment prices, labor costs, as well as overhead costs for facilities, equipment parts and operational strategy using a bottom-up approach. This manufacturing cost should be distinguished from the selling price of a MEA, which would additionally include markup, selling, general, and administrative expenses. The methodological framework of the model will be described in the next chapter, followed by a description of the scenario and the operation of the production. Subsequently, the considered materials and the process chain will be described. Finally, the introduced model will be applied to two industrial machinery configurations to determine achievable annual production throughputs and their effects on MEA cost.

2.1 | Model Methodology

The basis for this study is provided by the TCO framework introduced by Nold, in which the TCO of a product is determined by the sum of cost of ownerships COO of the production line. Within this, the COO of each production step k is calculated and summed up to yield the TCO of the product (Equation 1) [22].

$$TCO = \sum_{k=1}^N COO_k \quad (1)$$

The COO is governed by the E35 standard, issued by the “Semiconductor Equipment and Materials International” (SEMI) in Equation (2). It consists of the sum of all costs over the lifetime of an equipment, which includes fixed costs F , recurring costs R and all occurring scrape costs S . This sum is subsequently divided by the product of the lifetime of the equipment L , the annual throughput capacity of products TP , the total utilization TU as well as the product yield PRY . Fixed costs F are further broken down into the investment of the equipment as well as building infrastructure. The recurring costs R include all costs during the lifetime of equipment. This includes the necessary labor, utilities, (replacement-) parts, process consumables and the waste disposal of unused material [21].

$$COO = \frac{F + R + S}{L \times TP \times TU \times PRY} \quad (2)$$

Following the SEMI E10 standard, TU is described as the ratio of productive time t_p and the total time t_{tot} (Equation 3) [26]. t_p describes the time during which the equipment is running and producing the desired product. For t_{tot} , the time of a whole year (8760 h) will be considered. To connect TU to the SEMI E10's operational utilization U_{op} a scenario utilization U_s is introduced to account for the nonscheduled time of each work shift scenario which is outside of the regular worktime.

$$\text{TU} = t_p/t_{\text{tot}} = U_s \times U_{\text{op}} \quad (3)$$

with $U_s = t_{\text{op}}/t_{\text{tot}}$ with $U_{\text{op}} = t_p/t_{\text{op}} = A_{\text{op}} \times \text{OE}$

U_{op} is calculated by the operational uptime A_{op} and the operational efficiency OE, whereas A_{op} defines the ratio of the time the equipment can be run in comparison to the available time of operations. This is seen in the ratio of equipment uptime t_{eq} and operations time t_{op} in Equation (4). The difference between time t_{eq} and t_{op} accounts for scheduled and unscheduled downtimes. In this work only scheduled downtimes due to maintenance and the change of roll materials are considered. With this A_{op} represents the time fraction the machine is available for production based on the operation concept of a single machine [26].

$$A_{\text{op}} = t_{\text{eq}}/t_{\text{op}} \quad (4)$$

OE on the other hand, is defined by SEMI E79 and describes how well the available equipment time is used in combination with other processes (Equation 5). For this t_{eq} consists of the productive time t_p but also downtimes due to standby t_{sby} and engineering t_{eng} . In this work only t_{sby} due to the incompatibility with other process steps will be considered [27].

$$\text{OE} = t_p/t_{\text{eq}} \text{ with } t_{\text{eq}} = t_p + t_{\text{sby}} + t_{\text{eng}} \quad (5)$$

Furthermore, the presented methodology must be adapted to address limitations imposed by the use of R2R processes. Due to the coupling of multiple process steps, a superposition of individual steps is insufficient. Addressing these limitations requires several key extensions.

First, multiple parallel process chains that converge at specific points along the main production chain must be considered. This necessitates the representation of the production process as a directed graph instead of a linear chain of individual steps.

Second, yield loss propagation requires special consideration. While SEMI E35 mentions the need for defect tracking, it does not address the inherent limitation of removing yield losses after the process step in which a defect initially occurred [21]. Due to the nature of R2R processes, sections with identified defective material cannot be easily removed from a roll and are therefore passed on to subsequent process steps. Only when roll material is converted into individual products, or when roll material is combined with individual units, can downstream value addition be prevented. This increases the value of the discarded sections and leads to a reduction in effective throughput of non-defective parts, both of which must be accounted for. Similarly, when combining two or more rolls containing defective sections to create a combined material, the statistical distribution of the

defects determines which share of the combined material needs to be considered as yield loss. In this work, the combined yield is determined using a mean yield propagation, calculated as the multiplicative product of individual material yields, analogous to yield calculation for consecutive process steps.

Third, tolerance considerations present a similar challenge. Generally, tighter tolerances require higher equipment investment costs but reduce material consumption in manufacturing the final product [28]. This is also the case for R2R processes and high value coatings with a designed product width. Tolerances of subsequent production steps must be added on top of the product width. In a cost model, these requirements must be propagated back to the corresponding coating step and be reflected in increased material usage.

Finally, the specific consumable cost must be adapted according to the annual demand determined in the cost calculation [29]. This approach inherently captures the reduction of unit prices with higher order volumes within this proposed continuous process cost of ownership (CPCO) model. Figure 1 depicts the structure of a single process step k within the CPCO framework, showcasing the compatibility between the adapted TCO approach and PBCM as described by Field et al. [23]. The diagram illustrates how the operations model (operating hours, downtimes) governs the interaction between process parameters (material flow, product yield) and financial calculations (equipment costs, consumables, labor) to determine the COO for each process step.

2.2 | Scenario Assumptions

Within this study, the final cost of a MEA is linked to a specific scenario, which specifies key production process assumptions. In this work an indirect decal process route is considered and later described in Section 2.3. Two types of production scenarios are proposed, reflecting the variance of current fuel cell production installations [8]. The first is a research and development (R&D) setup with one 8-h shift per day, while the other consists of an industrial pilot plant with three shifts per day. The number of shifts per day affects the U_s , with more shifts enabling a higher utilization of the annual available time. The machinery configuration is tailored to each scenario type, as outlined in the following section. Both configurations are based on industrial machinery at the Fraunhofer ISE research labs. While the R&D scenarios use the equipment as is, the pilot plant scenarios employ a reconfigured setup for higher throughput. Wei et al. describe that process yields improve through “learning by doing” as annual throughput increases [17]. Given the industrial-grade machinery used in both scenarios, the throughput-dependent yields reported by Wei et al. are applied to both machinery configurations. The assumed yields are listed in Table 1 and are kept constant within each type of production scenario, independent of batch length.

The decal process route requires a transfer process, in which anode and cathode CL are hot laminated onto a proton exchange membrane (PEM). To reduce waste, it is necessary that the length of the produced CL rolls matches that of the roll of the PEM. Consequently, the batch length of all processes must be a multiple of n spliced membrane rolls. It is assumed that a maximum of five PEM segments of 250 m each can be spliced, resulting in a

TABLE 1 | Parameter specifications for production scenarios in research and development (R&D) and industrial pilot plant settings.

Production scenario		R&D	Pilot plant
Production time:	Working days per year ^a	251 (8 h)	355 (24 h)
	Fulltime equivalents (FTE)	1	5
	Scenario utilization, U_s	22.9%	97.3%
	Number of spliced PEM rolls ^a	1–2	1–5
Process yields:	Ink loss per batch ^a	1 L	1 L
	CCM yield [17]	91%	94%
	GDL yield [17]	96%	99%
	SG yield [17]	98%	99.5%

^aParameters are based on author assumptions.

batch length of up to 1250 m. Due to handling limitations in the R&D scenario only a maximum of two spliced PEM segments are assumed, corresponding to a batch length of up to 500 m.

The mixing of ink is assumed to be a daily batch process, producing only the necessary amount of ink for CL coating, including an ink loss of 1 L for both R&D and pilot plant machine configurations. This accounts for losses during the mixing and coating processes due to dead volumes in the coating equipment as well as remaining ink on tubing and vessel walls. Since the vessel walls are assumed to contribute only a minor fraction to the dead volume, the same volume is considered for both machine configurations, which are assumed to only differ in vessel size as described in the following section. All scrapped ink and subsequent yield losses of catalytic material are assumed to be recycled, recovering 70% of the platinum raw material price [30]. When recycling CL, the model considers only the active area and excludes additional coated area resulting from manufacturing tolerances. The recycling of ionomer is investigated in the literature, but as it is still an emerging field, it is not considered in this work [31]. Similarly, all other scrapped MEA materials are assumed to have no recoverable value.

Other general assumptions concern the number of fulltime equivalent (FTE), which defines the number of hired personnel for a given position. It is determined for each production scenario by the ratio of available hours of a laborer to the total hours of the scenario. In case of a fractional FTE, the number is rounded down to the nearest integer and the remaining hours are considered as overtime. All surcharges on the salary are taken from IG Metall and the German federal statistical office [32, 33]. In this model, only the positions of operators and supervisors are considered, for which salary data are taken from the International Labour Organization [34]. The cost of the cleanroom facility is mainly defined by the required footprint of the machinery considering additional handling space around the machinery. The cleanroom itself is assumed to be a basic cleanroom of ISO 7, with a cost share of 2112.37€₂₀₂₀ m⁻² [35]. To estimate the total building size, additional areas for administration, support and logistics are considered resulting in a total building size 45% larger

than the initial facility footprint [22]. The cost of capital for the investments in equipment, facilities and buildings is determined by the weighted average cost of capital (WACC). It is set to 9.3% considering an automotive sector [36].

Finally, all cost values presented are expressed in 2025 Euros. If a price was given in a different currency it is converted to Euro by the mean currency exchange of the given year and subsequently adjusted to the year of 2025 via the harmonized consumer price index of Germany [37]. The details of the conversion as well as all further assumptions can be found in Table S1.

2.3 | Processing Steps

The manufacturing of a fuel cell can be described as a set of production steps, each producing an intermediate product. For the MEA, a total of seven layers must be manufactured and assembled giving it the name of MEA_{7L}. This study focuses on the indirect production route given its process robustness [38]. The investigated process spans from the mixing of consumables like catalyst powder, ionomer and solvents to producing MEA_{7L} sheets, cut from the roll. The detailed production process includes the following steps, illustrated in Figure 2:

1. Ink mixing of the consumables—Process B
2. Coating and drying of the ink to create a CL on decal—Process B
3. Transfer of the anode and cathode CL onto a PEM to form a catalyst-coated membrane (CCM)—Process C
4. Preparation of the CCM- and the sub-gasket (SG) by cutting the roll material into individual pieces—Processes D and E
5. Application of the SG onto the CCM via a set of vacuum rollers to create a MEA_{5L}—Process F
6. Preparation of the gas diffusion layer (GDL) by cutting the roll material into individual pieces—Process G
7. Application of the GDL pieces onto the MEA_{5L} to create the MEA_{7L}—Process H
8. Cutting of the MEA_{7L} roll into individual pieces—Process I

Alternative production routes are discussed in the literature. Instead of the indirect decal route, the CL can be coated directly onto the PEM or the GDL [39]. In addition, different sealing options are available as presented by Ye et al. [40]. This also brings a variety of technical solutions for the application of the SG. One approach is given by the patent US2011/0151350A1 presented in the works of Heimes et al. [15] as well as James et al. [24]. This approach has the drawback of discarding a large part of the CCM roll while it is transformed to a MEA_{5L}, which can be omitted by the approach considered in this work. Here the use of vacuum rolls in sequence enables the creation of a gap between every CL and with this reducing the required area of CCM roll per MEA_{7L}. Focusing on the subsequent production step, both publications show different methods for applying the GDL to the MEA_{5L}. While James et al. [24] consider an intermittent approach to bond the GDL via the ionomer of the CL, Heimes et al. [15] present a continuous process with the application of a pressure sensitive

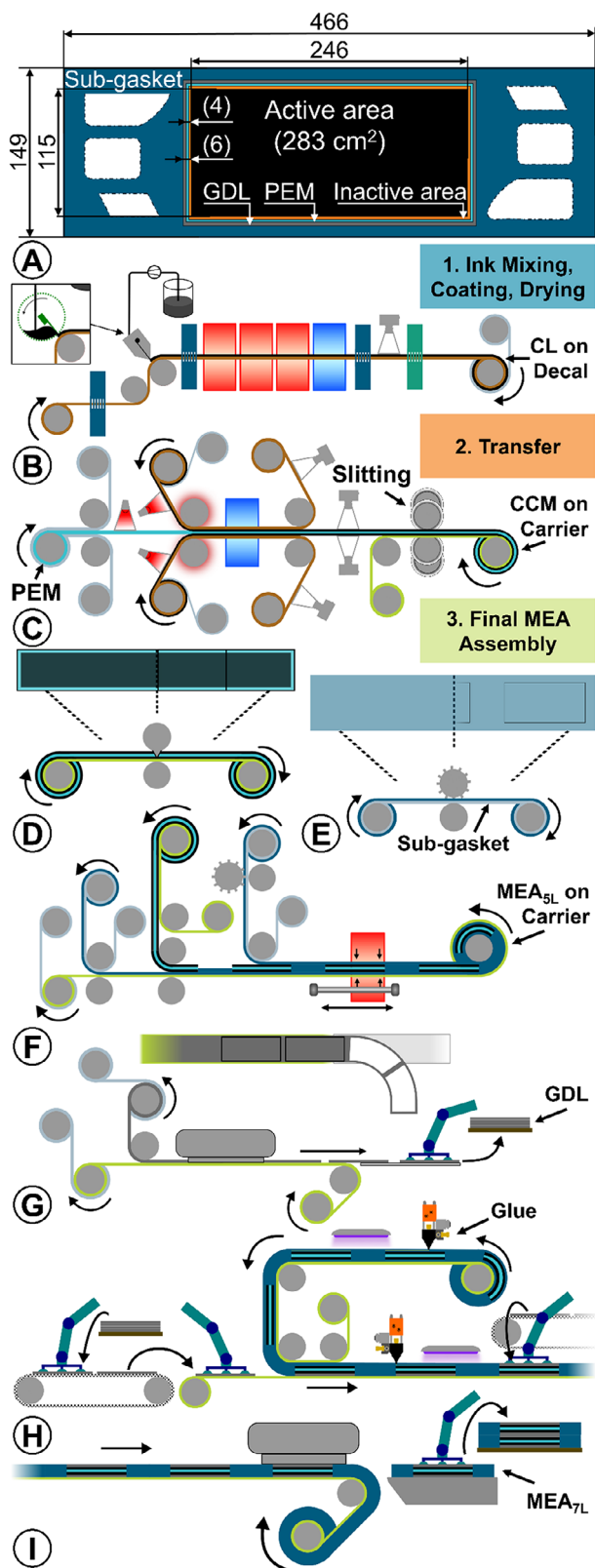


FIGURE 2 | (A) Schematic of the membrane electrode assembly (MEA) design [41]. (B–I) Process steps for MEA_{7L} manufacturing: catalyst ink preparation and coating of catalyst layers (CL), transfer of the CL onto the membrane (PEM) to produce the catalyst-coated membrane (CCM) on a carrier foil, processing of the CCM in the final MEA assembly by adding the gas diffusion layer (GDL) in reference to OPTIMA life science GmbH.

adhesive to bond the GDL to the MEA_{5L}. A similar approach with a UV curing adhesive is considered in this work but in an intermittent operation.

The production chain is based on the underlying cell design of the ZSW Generic Stack, which is shown in Figure 2A [41]. The design specifically declares the SG to overlap with the PEM, creating an active area in the middle of the PEM. To ensure a homogeneous coating of anode and cathode CL inside this active area, tolerances around it must be considered, creating an area of inactive CL at the rim, which is also part of the final cell but excluded from the electrochemical reaction, since it is covered by the SG. For the manufacturing of the MEA_{7L} the long axis of the Generic Stack is chosen to be the processing/machine direction (MD). This reduces the roll width and subsequently the investment cost of the later described final MEA machine. A change of process direction by 90° is investigated for the CCM process, resulting in a change of MD and the cross direction (CD). This requires a wider coating but on the other hand accommodates more individual CLs per roll. All roll materials are assumed to be purchased in standard configurations, as provided by suppliers for R&D scenarios, leading to scrapped materials if the required dimensions of the Generic Stack are not met. In contrast, for pilot plant scenarios, the order volume of materials is assumed to exceed suppliers' minimum requirements for customization. The purchased rolls can therefore be produced with matching requirements, minimizing slitting waste. An overview of the widths is given in Table 4 in Section 2.5.

Except for the mixing of the ink, every processing step is designed to be operated in a R2R configuration, which promises to increase throughput [39]. For every machine a set of operator and supervisor positions is assumed. A detailed overview will be given in the results section. Similarly, several downtimes of the machinery are assumed which halt the production and in effect lower the A_{op} of the machinery. These include the following:

- Yearly maintenance of one working day.
- Weekly cleanup of 4 h.
- Daily preparation of the machines of 2 h.
- Change of rolls of half an hour.

2.3.1 | Ink Mixing Machine

The first production step considered in this work is the mixing of ink. It is assumed to be performed in parallel for anode and cathode inks in separate devices in a daily batch operation. In this process the consumables of platinum on carbon powder and ionomer solution are mixed with a solvent combination. These solvent mixtures can vary depending on the use case and are closely linked to the desired coating technology [42]. For every batch, a loss of 1 L of ink is considered. The mixing device comprises two components: a larger stirred vessel for holding the bulk ink volume and a smaller high shear disperser for achieving the desired particle sizes. For R&D scenarios, the vessel can hold up to 4 L, while the vessel in pilot plant scenarios is assumed to hold up to 100 L. Since only the stirred vessel is assumed to require scaling, no additional investment costs are considered for the pilot plant version.

TABLE 2 | Parameters for the catalyst layers (CL) coating process.

				Cathode	Anode
Pt-loading ($\text{mg}_{\text{Pt}} \text{cm}^{-2}$)				0.4	0.05
Coating technology	RSP	—	—	Interm.	Conti.
	—	SDC _{int}	—	Interm.	Conti.
	—	—	SDC _{con}	Conti.	Conti.
Discarded startup prints	4 Screen rotations ^a	4 m ^a	4 m ^a	—	—
Coating tolerances—MD	80 μm^{a}	4.7 mm [48]	—	—	—
Coating tolerances—CD	80 μm^{a}	3.6 mm [49]	3.6 mm [49]	—	—
Transfer tolerances	—	—	—	—	400 μm^{a}
CCM cut tolerances	—	—	—	200 μm^{a}	200 μm^{a}
Sub-gasket application tolerances	—	—	—	400 μm^{a}	400 μm^{a}

Note: Process tolerances necessitate additional area around the active area of the CL. Listed tolerances apply to the entire width or length of the CL.

^aParameters are author assumptions based on machine supplier feedback.

As reported in previous publications, the chosen processing parameters can have a significant effect on the particle size distribution, viscosity and, consequently, on the homogeneity and performance of the CL [43, 44]. For cost calculation purposes, it is assumed that a one-day preparation time is sufficient to achieve the necessary ink properties. Due to the daily batch operation, the OE is calculated based on the required ink volume relative to the maximum possible filling volume of the mixing vessel.

2.3.2 | Coating and Drying Machine

In the considered indirect process route, the CL is coated onto a decal foil, with the goal of coating an anode and cathode CL with loadings of 0.05 and 0.4 $\text{mg}_{\text{Pt}} \text{cm}^{-2}$, respectively (Figure 2B). Due to low utilization of the coating line in R&D scenarios, it is assumed, that both anode and cathode CL are produced on the same machine consecutively, while in pilot plant scenarios a machine is necessary for each CL type.

For the coating technology, a range of coating and printing methods are available with different requirements to the used ink, for example, inkjet printing, spray coating, SDC, or rotary screen printing (RSP). The latter two being the focus of this study. Regarding the ink composition, SDC utilizes a closed ink reservoir, which opens the possibility for the use of low boiling point solvents. A typical solvent mixture consists of 1-propanol and DI-water as presented by Mauger et al. [45]. On the other hand, RSP works with an open ink reservoir, necessitating inks with high boiling point solvents such as ethylene glycol and 1,2 propanediol presented by Ney et al. for flatbed screen printing (FSP) [42]. In addition, the screen must be considered as a wearing component, which needs constant replacement after 100 000 linear meters of coating as suggested by a commercial screen manufacturer. In practice, the coating of CL via SDC is performed at speeds of 1 m min^{-1} or lower [45–47]. On the other hand, reports of SDC battery inks show that speeds of 50 m min^{-1} are possible [48, 49]. RSP is still novel in the domain of fuel cells, so no production speeds could be identified in the literature, but comparing to FSP speeds of 18 m min^{-1} have been reported [9].

With this a base processing speed for the coating of 10 m min^{-1} is assumed. In addition to unforeseen yield losses described in Table 1 startup- and shut down scrape prints are considered due to coating instabilities at the beginning and end of a production. For RSP 2 × 2 screen rotations are assumed, resulting in eight CL and 2 × 2 m for SDC, which are removed before the CL are passed to the next process step.

The subsequent drying of the coated CL is a crucial step and can have a significant influence on the microstructure of the coating and the performance of the CL [50]. A wide range of drying methods is available ranging from hot plate, convection, and laser drying, with convection drying assumed to be the industrial standard [15]. Due to this variety, the optimal drying profile and associated drying time must be determined separately for each ink composition and drying method to ensure optimal CL performance. However, measuring convection drying time was not feasible at the facilities of Fraunhofer ISE. Therefore, to approximate the minimum drying time for the cost model, this study proposes determining the drying time for SDC and RSP inks using a hotplate. Subsequently, the measured times are adapted for a convection dryer. The experimental setup and conversion to the required drying time t_{dry} is described in Figure S1.

Calculating the length of the convection dryer, a warmup and cooldown phase L_{const} of 0.5 m is considered due to limitations of a convection dryer in comparison to a hotplate presented by Ney et al. [53]. Combined with the coating speed v_{coat} the length of the dryer L_{dry} is defined by Equation (6).

$$L_{\text{dry}} = L_{\text{const}} + v_{\text{coat}} \times t_{\text{dry}} \quad (6)$$

Manufacturing tolerances, in this context, add material to the CL, that does not contribute to the performance of the CCM described as inactive area in Figure 2A. Depending on the selection of the coating method and subsequent processes, different tolerances need to be accounted for in MD and CD. In the case of continuous (con) coating, no gaps are produced between each single CL in MD. This results in the complete coverage of the 8-mm long SG overlap area on the membrane with CL material, which will later be covered by the SG for sealing. In comparison, RSP and

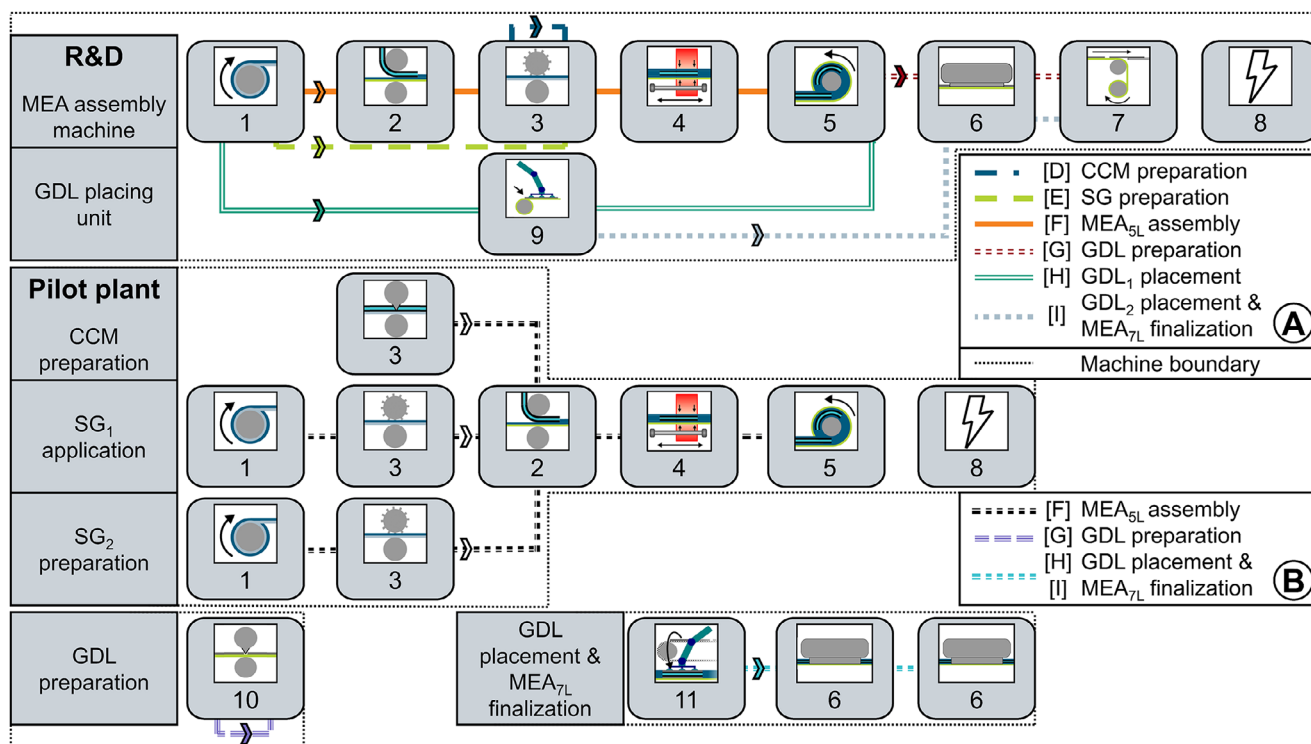


FIGURE 3 | Machine configurations for the “final MEA assembly.” Module numbers correspond to the elements in Table 3. (A) Machine configuration for R&D scenarios, with each module (1–9) used once to perform all process steps (D–I) of Figure 2. (B) Machine configuration for pilot plant scenarios, with each module dedicated to a single process to enable parallel production in accordance with feedback from OPTIMA life science GmbH.

intermittent SDC (SDC_{int}) can produce a gap in MD, resulting in smaller tolerances than continuous coating. In addition, it is assumed that during the transfer of the electrodes onto the PEM at least one electrode roll must be coated continuously to prevent misalignments between intermittent CCM patches. This is caused by the transfer rollers pressing the webs together, making MD alignment adjustments infeasible. On the other hand, misalignments in CD can be adjusted by web guides requiring only an assumed tolerance of 400 μm as listed in Table 2.

Here, the anode is chosen to be coated continuously. Every successive production step adds additional tolerances, including the SG application, which must be considered already during the design of the CCM. The assumed tolerances are listed in Table 2. In total, the considered tolerances of 0.9%–7% in relation to the active area can be considered as modest comparing to an inactive area of 15% presented by Wei et al. [17].

2.3.3 | Transfer Machine

The transfer process joins the anode and cathode CL (Figure 2C). A calendar roll exerts pressure and heat on the sandwich of CLs and the PEM bonding the ionomer of the CL with the PEM [38]. Simultaneously the width of the purchased membrane material, if deviating from the required dimensions of the MEA, will be slitted to match the design. For this a standard roll width of 360 mm is assumed in the R&D scenario, which can be further slitted to two separate rolls. Combined with a width of 123.3 mm of the CCM this results in a membrane waste of 31.7% for the slitting in MD only.

Process yield losses are attributed to the transfer process by assuming the CCM yields provided by [17]. These are listed in Table 1 and include yield losses from the mixing of the consumables up to the transfer process. Notably, removing these defective CCM parts from the roll after the transfer is assumed to be impractical, requiring them to be processed through the subsequent manufacturing steps.

2.3.4 | Final MEA Assembly Machine

The final MEA machine will convert the CCM to a MEA_{7L} in the process steps D–I, displayed in Figure 2. These include the preparation of the CCM (Process D), SG (Process E), and GDL (Process G) by cutting the roll material into individual pieces while maintaining them on a roll. In addition, for the SG, the contour of the active area is cut into the SG material. For the GDL and CCM it is assumed that they are not available with a dedicated protection foil to which the material is attached, requiring a carrier material (green web in Figure 2) to retain the individual pieces and thereby enable continuous R2R processing.

Defective GDL sheets are assumed to be removable from the process directly after cutting and GDLs only need to be placed on the anode and cathode side of defect-free MEA_{5L}. Before this step the prepared CCM and SG rolls are hot sealed together (Process F). Subsequently, a UV-curing glue is applied on the SG and activated (Process H). After the placement of both GDLs, the final MEA_{7L} can be cut into separate pieces concluding the manufacturing process (Process I). Only at this final step defective

TABLE 3 | Module description and specifications for the “final MEA assembly machine.”

#	Machine element	Number of modules R&D Pilot plant	Costs share (m) ^a	Line speed (m min ⁻¹)	Module length (m)
1	Unwinding	1 2	7	—	1
2	CCM positioning (F)	1 1	19	14	2
3	Kiss-cut (D, E)	1 3	11	14	2
4	Hot sealing (F)	1 1	15	14	2
5	Un- and rewinding	1 1	7	—	2
6	Flatbed cutting (G, I)	1 2	29	8.78, 6.99 ^b	2
7	Rewinding	1 0	4	—	1
8	Power supply	1 1	8	—	1
9	GDL placement (integrated) (H)	1 0	20	6.99	2
10	GDL preparation (G)	0 1	20	20	3
11	GDL placement (separate) and MEA _{7L} finalization (H)	0 1	80	13.98	7

^aModule cost shares are relative to the original investment cost of the machinery at the research labs at Fraunhofer ISE. All numerical values represent author estimates informed by technical feedback from OPTIMA life science GmbH.

^bAverage flatbed cutting line speed depends on the processed material.

CCMs are assumed to be removed as MEA_{5L} from the production chain. An overview of the steps in which yield loss can be removed from the production chain is provided in Table 7 in Section 3.3 for R&D scenarios and in Table S3 for pilot plant scenarios.

The machinery facilitating all processes is subdivided into modules, where every module is dedicated to one process. This is shown in Figure 3 for the machine configuration of the R&D as well as the pilot plant scenarios. The machine of the research labs at Fraunhofer ISE represents the basis of this analysis, which consists of the Modules 1–8 in the R&D configuration. For the production cost analysis, Module 9 is an extension to the original machinery, assumed to cost an additional 20% relative to the investment cost, resulting in a total cost of 120% with respect to the original machinery investment cost for the R&D machinery. The R&D configuration is integrated into a single machine to reduce the footprint and investment costs. This comes with the drawback that multiple processes require the same module. This can be illustrated by Processes D and E, which both use Module 3. Due to these overlaps, every process must be performed separately on the machine resulting in six consecutive passes of materials until all processes are executed to finalize an incoming CCM roll to MEA_{7L} sheets. While the operational line speeds of every process in a module are given in Table 3, the average throughput to convert a CCM to a MEA_{7L} is greatly reduced, as investigated in Section 3.3.

To alleviate this bottleneck in the MEA_{7L} production and enable parallel processing of all six steps, a machine redesign is proposed by assessing module costs (Table 3) and duplicating modules as necessary. This results in three separate machines operated in parallel, as shown in Figure 3B. The first machine performs the GDL preparation by cutting the GDL roll into individual pieces. This step is isolated from the main production line to prevent contamination of other MEA_{5L} parts by loose fibers. The second machine performs the CCM and SG preparation by cutting the roll materials into individual pieces and simultaneously applying the

SG to the CCM in an inline process. After hot sealing, the MEA_{5L} is rewound and passed to the final machine. The third machine transforms the MEA_{5L} into a MEA_{7L} by placing the GDL onto the prepared MEA_{5L} and then cutting the SG contour and ports to produce individual MEA_{7L} sheets.

2.4 | Ink and Materials

For the cost calculation, the cathode ink is set to be comprised of 50 wt% Pt on carbon, a 25 wt% ionomer dispersion in water and the solvent mixtures described above, formulated with an ionomer-to-carbon ratio (I/C) of 0.8. The anode ink consists of 20 wt% Pt on carbon with the same I/C of 0.8. To enable direct cost comparison between coating methods, both screen printing and SDC inks are designed with a solid content of 17 wt%.

2.4.1 | Sample Preparation for Performance Validation

Evaluating the electrochemical performance of MEA_{7L} with different Pt-loadings, cells are experimentally prepared via FSP as described in a previous publication [9]. For the purpose of cost calculations, these are assumed to exhibit the same performance as CL produced via SDC. The same solvent mixture as described above for both RSP is used due to the similarity to FSP in combination with 47 wt% Pt on carbon (Elyst Pt50 0550, Umicore AG & Co. KG), 25 wt% ionomer dispersion in water (Aquivion D79-25BS, Sigma Aldrich Chemie GmbH) [54].

The ink with an I/C of 0.8 is prepared by first evaporating the water from the ionomer solution and subsequent ball milling (Dispermat CV3evo, VMA Getzmann) at 7000 rpm for 30 min using 0.8–1 mm balls. Screen printing is performed using a 200 mesh (wires per inch) with 40 μm wire diameter, followed by drying at 150°C in a convection dryer (Reflow 548.10, SEF). To

TABLE 4 | Considered parameters to calculate the consumable raw material price c_j .

Consumable	Composed materials	This scenario	Source	Roll width (R&D Pilot plant) (mm)
Catalyst powder	Pt content	20/50 wt%	Assumption	—
	Material cost	1364\$ ₂₀₂₅ troy oz ⁻¹	[58]	
	Markup	2%	[24]	
	Carbon	116\$ ₂₀₁₆ kg ⁻¹	[24]	
Ionomer dispersion	Ionomer content	25 wt%	Assumption	—
	Equivalent weight	790 g mol ⁻¹	Assumption	
	Material cost	71.01€ ₂₀₁₄ kg ⁻¹ _{1100EW}	[61]	
	Markup	10%	[61]	
	Water	2.71€ ₂₀₁₈ m ⁻³	[70]	
Solvents	Index price	Solvent specific	[71]	—
Membrane	Thickness	15.5 μm	Offer specific	360 123
	ePTFE	6.00\$ ₂₀₁₆ m ⁻²	[24]	
	Cerium oxide	1.69\$ ₂₀₂₁ kg ⁻¹	[72]	
	Equivalent weight	790 g mol ⁻¹	Assumption	
	Material cost	124.56€ ₂₀₁₄ kg ⁻¹ _{1100EW}	[61]	
	Backing film	0.50 \$ ₂₀₁₆ m ⁻²	[24]	
	Sub-gasket	Polymer	Polyethylene naphthalate (PEN)	Assumption
	Thickness	25 μm	Assumption	
	Material cost	5.52\$ ₂₀₂₄ kg ⁻¹	[73] (Tables S4 and S5)	
	Areal cost	0.18€ ₂₀₂₅ m ⁻²	Calculated	
	Glue thickness	15 μm	Assumption	
	Material cost	20\$ ₂₀₁₄ kg ⁻¹	[24]	
	Areal cost	0.37\$ ₂₀₁₄ m ⁻²	Calculated	
	Backing film	0.50\$ ₂₀₁₆ m ⁻²	[24]	
GDL	Material cost	1.89\$ ₂₀₁₆ m ⁻²	[24]	450 127
	Backing film	0.50\$ ₂₀₁₆ m ⁻²	[24]	
Carrier	Thickness	75 μm	Assumption	170 170
	Polymer	PET	Assumption	
	Material cost	1.38\$ ₂₀₂₄ kg ⁻¹	[71]	
	Areal cost	0.13€ ₂₀₂₄ m ⁻²	Calculated	
Decal foil	Thickness	75 μm	Assumption	170 123
	Polymer-content	65 vol% PTFE	Assumption	
	Material cost	13.51\$ ₂₀₂₄ kg ⁻¹	[71]	
	Areal cost	2.59€ ₂₀₂₄ m ⁻²	Calculated	

Note: Values from different years and currencies are converted to Euro and adjusted to the year of 2025.

achieve different loadings, multiple prints are conducted on top of each other to reach loadings from 0.16 to 0.42 mg_{Pt} cm⁻².

The transfer is performed by hot-pressing the CL onto a GORE-SELECT M775.15 membrane at 180°C and 1.2 MPa over a 20 cm² area for 15 min. Afterwards, the SG (CMC 61325) is applied and sealed at 90°C for 3 min. Before in situ characterization, GDL (Freudenberg H23C9) are added to each electrode. The mentioned consumables are assumed for the cost calculation in

combination with a 75-μm thick polytetrafluorethylene (PTFE) decal foil and a 75-μm thick polyethylene terephthalate (PET) carrier.

The in situ characterization is performed with a Baltic FuelCells liquid cooling quickConnect high amp test cell at 1.35 MPa cell compression and cell temperature of 80°C. The cells are conditioned at 100% relative humidity (RH) and 2 bar gas pressure. Initially, a constant current density of 1.5 A cm⁻² is

applied for 1 h followed by cycling between OCS, 0.6 and 0.4 V for 4 h. Polarization curves at 100% RH on both anode and cathode are recorded at 2.0 bar gas pressure with a volumetric flow rate of 23.0 slpm hydrogen and 5.0 slpm air, measuring from OCV and 0.2 V. The roughness factor (RF) is measured by cyclic voltammetry, ramping from 0.05 until 0.9 V at a rate of 100 mV s⁻¹ with 1 slpm hydrogen (anode) at 100% RH. Additional information on the in situ protocol is given by Schneider et al. [55].

2.5 | Consumable Price Modeling

The price of consumables serves as input to the TCO model. Given their crucial role in the current development of fuel cells, special focus is placed on modeling the price composition of the consumables [20, 24]. Since multiple scenarios are to be investigated, a fixed price for every consumable is insufficient. Therefore, a generalized learning curve approach is adopted to model the price evolution of the necessary materials [29]. Using this model, the mean price per unit $\bar{T}_j(N)$ of material j is determined as a function of the volume N as given in Equation (7). This framework assumes that fuel cell consumable suppliers operate at high production volumes, so that their raw material prices do not depend on the order quantities of individual CCM manufacturers. Under this assumption, the price of consumables can be divided into two components. A logarithmically decreasing processing price $\bar{P}_j(N)$, that includes processing costs as well as the supplier markup (Equation 8) and a fixed raw material price c_j . This approach allows the combination of data points from different suppliers and different material compositions, assuming compositional variations affect only the fixed material price and not the processing price.

$$\bar{T}_j(N) = a_j \times N^{b_j} + c_j \quad (7)$$

$$\bar{P}_j(N) = a_j \times N^{b_j} \quad (8)$$

$$\ln(\bar{P}_j(N)) = \ln(a_j) + b_j \times \ln(N) \quad (9)$$

The defining parameters a_j and b_j of the processing price are determined by linear regression via least squares of the logarithmic function of $\bar{P}_j(N)$ (Equation 9) [57]. To collect data points for the function $\bar{P}_j(N)$, the processing price $\hat{P}_{j,i}$ of datapoint i is calculated by subtracting $c_{j,i}$ from the total price $\hat{T}_{j,i}$. Here, $c_{j,i}$ is determined by the material combination of the datapoint. After the parameters of the function $\bar{P}_j(N)$ are determined, the model can be applied to estimate the consumable prices in the presented scenarios by calculating the parameter c_j based on the selected materials and combining it with the order volume-dependent processing price $\bar{P}_j(N)$. An exemplary calculation for a datapoint can be found in Table S2.

For platinum pricing in this work, the current price of \$₂₀₂₅ 1364 per troy oz (July 1, 2025) is utilized, along with a handling markup for platinum group metals of 2% [24, 58]. This price is considerably higher than the mean price of \$959 per troy oz over the last 10 years [58]. In addition, the price of ionomer is adjusted based on its equivalent weight (EW) according to James et al. [24]. Table 4 lists the considered parameters to calculate c_j as well as the assumed standard roll widths from suppliers.

Finally, to assess the robustness of the MEA_{7L} price a Monte Carlo simulation (MCS) with 10 000 iterations is performed for every scenario. As input, the 10 most influential parameters to the yearly cost of the CCM are considered and listed in Table S6. The price distribution of the selected parameters is assumed to be gaussian. For non-consumable parameters the distribution is defined with one-sigma set to 20% of the mean price [22]. For consumable parameters the logarithmic process price of Equation (9) is considered as random variable (Equation 10) and the standard deviation σ_j is determined via the linear regression to the dataset. The raw material price c_j is kept constant and with this the random variable $T_j(N)$ is defined via Equation (11).

$$\ln(P_j(N)) = \mathcal{N}(\ln(\bar{P}_j(N)), \sigma_j^2) \quad (10)$$

$$T_j(N) = \exp(\ln(P_j(N))) + c_j \quad (11)$$

3 | Results and Discussion

This section presents the cost analysis results progressing from consumables to complete MEA_{7L} production. First, the consumable cost structure is established, followed by an examination of the influence of coating parameter on CCM manufacturing costs. These results are then extended to the complete MEA_{7L} assembly. Finally, the influence of Pt-loadings on manufacturing cost, and electrochemical performance is analyzed to identify cost-optimal catalyst loadings based on beginning of life (BOL) experimental data.

3.1 | Price of Consumables

A specific focus was set on identifying the relationship between datapoints of preliminary supplier price quotations and recently published data. Figure 4 plots the specific cost of each datapoint against the order volume. To enable comparison across suppliers with different specifications, all data points are normalized to the scenario raw material price. Specifically, the raw material price $c_{j,i}$ for each data point is calculated, then adjusted the total price of the datapoint $\hat{T}_{j,i}$ to the scenario by subtracting $c_{j,i}$ and adding the scenario raw material price c_j . To differentiate quoted data from literature datapoints, these are presented in red and blue colors while data from Strategic Analysis (SA) draft publication of 2023 is marked in orange and violet colors [59]. In addition, in light colors the previous SA datapoints from 2018 and 2019 are shown [24, 60]. The fitted regression curve is presented in combination with the 95% confidence and prediction interval.

The literature data largely complements the data obtained by suppliers and the resulting regressions can be fitted to the combined datasets. In total 275 datapoints from 24 different sources could be obtained. Comparison of the datapoints of the 2018 and 2023 publications of SA shows that none of the price projections were reduced. Notably, projected prices for consumables based on PFSA polymers (Figure 4B,C) were increased in the later publication. However, when comparing the updated datapoints with quoted datapoints, which are plotted as plain ionomer masses without solution, the alignment improves compared to previous datapoints. This can be attributed to findings by

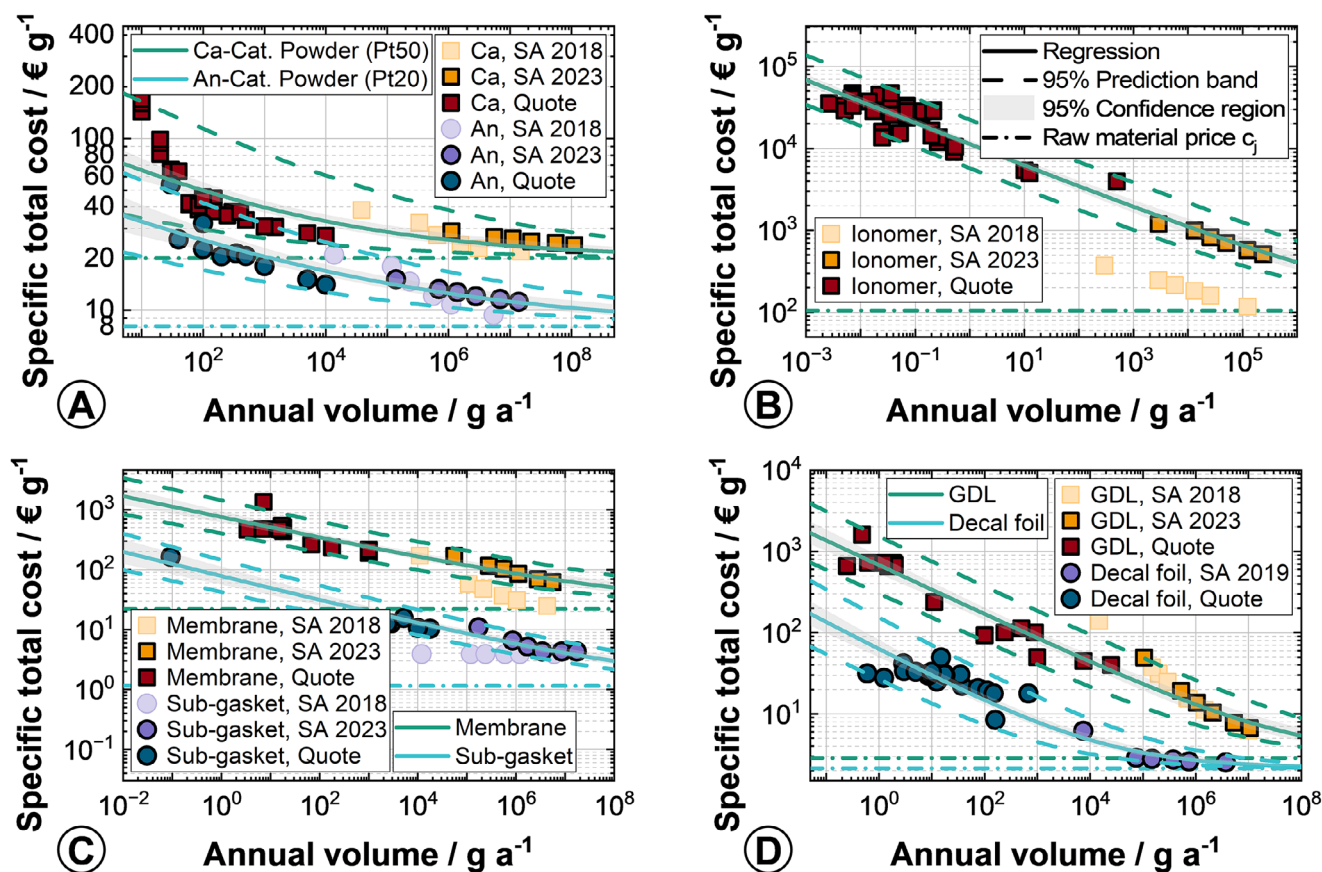


FIGURE 4 | Consumable price regression with the underlying datapoints of the most relevant consumables for PEM fuel cells. The specific total price is shown as function of the annual order volume. Shown are quoted datapoints as well as data from Strategic Analysis (SA) [24, 59, 60]. Horizontal lines represent the material price c_j . Linear regression is performed on outlined datapoints only.

TABLE 5 | Fitted data of the consumable price regression defining the parameters of Equation (7).

Consumable	Unit	a_j	b_j	c_j
An-catalyst powder (Pt20)	€ g ⁻¹	34.768	-0.149	8.081
Ca-catalyst powder (Pt50)	€ g ⁻¹	69.069	-0.182	20.03
Ionomer	€ kg ⁻¹	11 134	-0.261	104.3
Ethylene glycol	€ L ⁻¹	76.348	-0.325	0.7022
1-Propanol	€ L ⁻¹	64.026	-0.378	1.111
DI-water	€ L ⁻¹	5.3663	-0.0762	0.003452
1,2 Propanediol	€ L ⁻¹	36.138	-0.160	1.300
Membrane	€ m ⁻²	732.28	-0.175	21.85
Sub-gasket	€ m ⁻²	71.575	-0.182	1.142
GDL	€ m ⁻²	672.55	-0.303	2.844
Carrier	€ m ⁻²	14.937	-0.101	0.1360
Decal foil	€ m ⁻²	60.558	-0.340	2.122

Gebert, who stated that due to the specialized nature of PFSA ionomer, it cannot be viewed as a commodity polymer and thus cannot be expected to exhibit the price decreases comparable to other polymers like PTFE [19]. A small spectrum of applications additionally limits the production volume and with this the

opportunities for cost reductions. Also, the stated ionomer raw material price of 71.01€₂₀₁₄ kg⁻¹_{1100EW} needs to be taken with care, since this value is based on a 2014 analysis and may not reflect present market prices [61].

The catalyst powder (Figure 4A) shows one of the largest spans of the prediction interval. This can be explained by the proposition of James et al., that at low volumes the consumables are subsidized to enable market development market [24]. Additional bias might be introduced due to the requests for quotation originating from a research institution. This distorts the data, making it challenging to fit a simple linear regression. Nevertheless, even at 10 kg volume, the fitted price curve indicates that raw material costs account for more than 50% of the catalyst powder price, limiting opportunities for future reductions of the specific price. The overview of the price regression parameters of all consumables is given in Table 5.

3.2 | CCM Comparison

In the first scenario, intermittent SDC is investigated to produce a CCM via the decal transfer route with the pilot plant setup. Initially a coating and transfer speed of 1 m min⁻¹ is investigated, due to its relevance in current literature [45–47]. With a batch length of 1,250 m of CL/CCM based on five spliced membranes a throughput of 45 500 m²_{active} or 1.6 × 10⁶ CCMs per year is

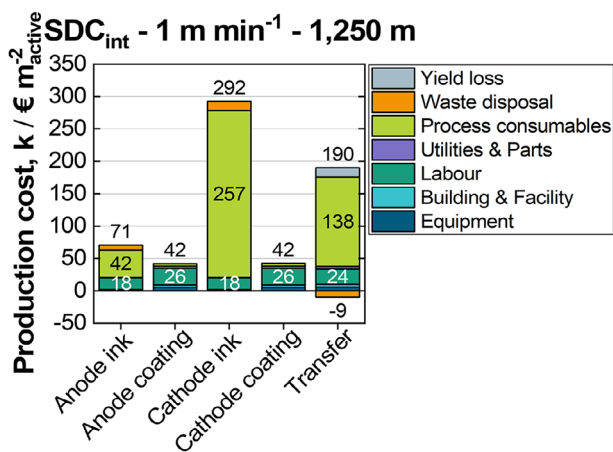


FIGURE 5 | Cost breakdown of a CCM production at 1 m min^{-1} and a batch length of 1250 m. Costs are allocated across each production step k .

achieved. The cost breakdown for each process step k is shown in Figure 5 with a total CCM cost of $640 \text{ € m}^{-2} \text{ active}$ including capital costs.

Most of the CCM costs stem from only two process steps, driven by the materials they introduce to the final CCM. In the cathode ink mixing process, the cathode catalyst powder accounts for 51% of the total consumable costs. The catalyst cost includes both the ink used in the final CCM and the discarded 1 L of ink for every batch, marked as waste disposal. The membrane, introduced in the transfer process, contributes another 33% to the total consumable costs. In the transfer step the CCM yield loss is attributed as well, leading to an additional cost of 14 € m^{-2} . However, 66% of the losses can be recouped with the recycling of Pt shown as the negative waste disposal bar. This results in a total consumables share of 71% to the CCM cost.

Labor costs contribute 18% to the final cost of the CCM, while costs for equipment, building, utilities and parts only play a minor role in this scenario. Also support materials like the decal foil for the indirect process route are included, indicating that from a production cost perspective the choice of the process route with direct or indirect coating does not play a major role. However, this conclusion must be evaluated while considering the restrictions presented in the following comparison of coating methods.

Investigating the volatility of the results via the MCS places the median CCM cost slightly higher than the deterministic price at $652 \text{ € m}^{-2} \text{ active}$. In addition, the distribution ranging from $564 \text{ € m}^{-2} \text{ active}$ to $783 \text{ € m}^{-2} \text{ active}$ for the 5% and 95% quantile, respectively, indicates a positively skewed distribution. The skewed distribution results from the logarithmic nature of the price distributions, which dominate the total price of the CCM. The full distribution is provided in Figure S3, and the 90% confidence range will be applied as error bars for each scenario.

For the comparison of the coating methods the base processing speed of 10 m min^{-1} utilized. These scenarios with an annual throughput of $384 \text{ 00 m}^2 \text{ active}$ again identify the consumables as the key cost driver for every coating method, as shown in Figure 6A. Contrary to the previous scenario, the share of labor

cost dropped to below 4% of the final cost. Due to the largest tolerances and consequently the largest amount of inactive area, the continuous SDC (SDC_{con}) shows the highest cost within the compared coating technologies. SDC_{int} and RSP require smaller tolerances, leading to a reduced material usage and cost of consumables.

To validate the observed effect of the tolerances, a scenario is conceived where RSP is assumed to have the same tolerances as a SDC_{int} process ($\text{RSP}_{\text{Extra-Tol}}$). This results in similar consumable costs as the SDC_{int} , strengthening the argument, that the considered tolerances are the main cause for the change in price. The analysis demonstrates that the added replacement parts for RSP as well as the difference of solvents and consequently the drying time and length contributes only a minor cost, provided the same yield and final CCM performances can be achieved. Notably, this only holds true, if the ratio of consumable costs outweighs the costs of buildings and equipment. At lower annual volume scenarios, the costs of added dryer length for RSP can outweigh the cost gains due to lower margins during the coating. On the other hand, the presented uncertainties determined with MCS indicate that consumable price variations can overshadow the cost differences between coating methods.

Adding to the already discussed scenarios of SDC_{int} , coating speeds of 50 and 100 m min^{-1} are investigated in Figure 6B to assess cost benefits at higher line speeds. In addition, the orientation of the processing direction is changed from 0° to 90° , which more than doubles the throughput from $1.4 \times 10^6 \text{ m}^2 \text{ active}$ at 100 m min^{-1} and 0° to $2.9 \times 10^6 \text{ m}^2 \text{ active}$ per year. Due to the increased throughput of the coating lines the number of mixing vessels is increased according to the required daily ink volume. For each scenario the CCM yield is adapted based on the data of Wei et al. [17]. The assumed dryer length for the cathode CL production is increased from 1.3 to 86 m based on Equation (6) and the experimental data shown in Figure S2. This is similar to convection dryer lengths used in lithium-ion battery production [62]. A clear trend toward reduced costs with increasing throughput can be observed, but since material costs already dominate the cost of the CCM, further reductions cannot be expected using current materials. Furthermore, the change in processing direction does not significantly reduce costs compared to increasing throughput, leaving few production-related options for further CCM cost reductions.

The evaluation of coating methods did not identify a clear pathway to significantly lower CCM costs. This suggests that other factors must be considered when selecting the coating technology. Achievable yields should be evaluated first, followed by tolerance analysis only if comparable yield levels are attained. In addition, the coating technology's impact on final cell performance and the degrees of freedom available for CL design must be assessed.

3.3 | MEA_{7L} Comparison

After the CCM manufacturing, the remaining production steps add the SGs and GDLs to the CCM to finalize the MEA_{7L}. This requires a set of six individual steps, as presented in Section 2.3, which are performed sequentially in the R&D scenarios on the same machine. The time of each process step as a function of

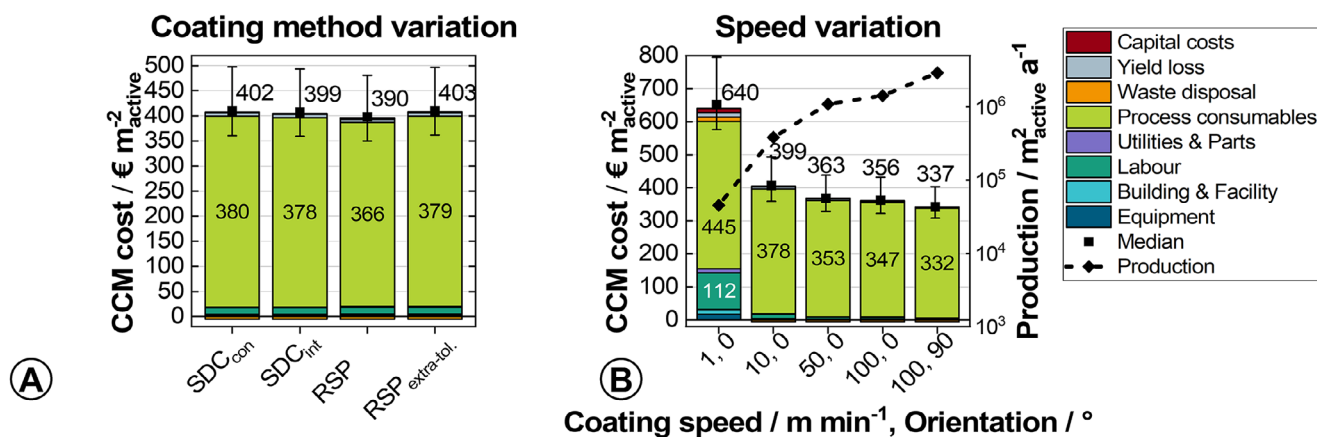


FIGURE 6 | Comparison of different catalyst-coated membrane (CCM) production scenarios. Error bars represent the 90% confidence range of a Monte Carlo simulation with 10 000 iterations. (A) Coating method variation at coating speeds of 10 m min⁻¹ and a batch length of 1250 m. (B) Variation of the coating speed, as well as the process orientation of the CL, leading to different production throughputs.

TABLE 6 | “Final MEA machine”. Process times, including roll changes.

#	Process	<i>n</i> : 1 Roll (250 m)	<i>n</i> : 2 Spliced rolls (500 m)
D	CCM preparation	0.80 h	1.10 h
E	SG preparation	1.05 h	1.59 h
F	MEA _{5L} assembly	1.05 h	1.59 h
G	GDL preparation	1.54 h	2.59 h
H	GDL ₁ placement	1.32 h	2.14 h
I	GDL ₂ placement and MEA _{7L} finalization	1.59 h	2.69 h
Σ	Total time	7.35 h batch⁻¹ (0.57 m min⁻¹)	11.69 h batch⁻¹ (0.71 m min⁻¹)

Note: Capital letters refer to the process shown in Figure 2.

the batch length is given in Table 6. The indicated times include the processing time as well as the necessary time to change the materials for the next production step. Each process step is assumed to process one whole batch of CCM, while the GDL preparation is performed on *n* spliced GDL rolls of 550 m. By summing the time of all processes and dividing it by the CCM batch length yields the average processing time to convert a CCM roll to individual MEA_{7L}.

Doubling the batch length, can increase the average production speed by 25%. However, even at an average production speed of 0.71 m min⁻¹, the final MEA machine represents the bottleneck of the entire MEA_{7L} production. This is evident from the operational uptime *A*_{op} in Table 7. The increase in batch length raises *A*_{op} for all roll-processes, but the gain is limited to a maximum of 12%. All process steps of the final MEA machine, excluding the GDL preparation are at full operational efficiency OE, highlighting the bottleneck of the process chain. Minor improvements could be made to the operations strategy, by reducing the dedicated time of the GDL preparation, but this was neglected in this work. Regarding the removal of yield loss, it becomes apparent, that the

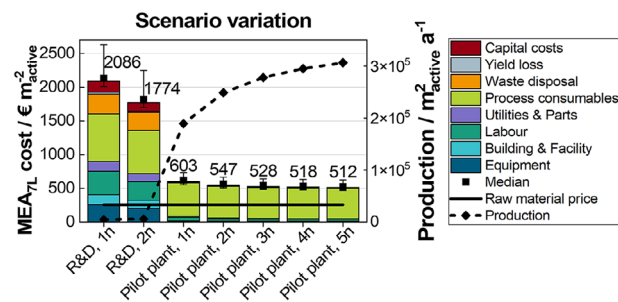


FIGURE 7 | Comparison of the seven-layer MEA (MEA_{7L}) costs of different production scenarios and batch lengths for *n* spliced PEM rolls, each 250 m in length. Error bars represent the 90% confidence range from a Monte Carlo simulation with 10 000 iterations.

ability to remove defective parts only at the end of the production chain increases the burden on the most limiting process steps by lowering the effective throughput for still intact MEAs.

In the pilot plant setup, the total sum of assumed labor positions increases from 15 to 20 positions as seen in Table 7 and Table S3. However, due to the FTE of five instead of one in these scenarios, the number of personnel increases by more than sixfold. Similarly, the building footprint increases from 1500 to 2500 m². Combined with the assumption of handling up to five spliced rolls, *A*_{op} of the final MEA machine processes rises to 75%. Together with three shifts per day, the capacity for MEA_{7L} production increases significantly from 4590 to 306 000 m²_{active} per year (equivalent to 0.3 MEA_{7L} up to 20.5 MEA_{7L} per minute). This is shown in Figure 7 and results in a distribution of fixed costs over a larger number of MEA_{7L}. This explains the reduced shares of labor, capital, equipment, building and utilities costs for the pilot plant scenarios compared to the R&D scenarios. As shown in the previous CCM calculations, at sufficient production volumes, the cost of the MEA_{7L} is mainly dominated by the consumables. Still, cost reductions through economies of scale can be identified, which lowers the cost of a MEA_{7L} by 75% from 2,086€ m⁻²_{active} to 512€ m⁻²_{active}. This is accompanied by an increased share of consumables, both used and wasted, rising from 48% to 90% of total costs.

TABLE 7 | Key performance indicators, including operational uptime A_{op} and operational efficiency OE as well as assumptions of each machine in the R&D scenario.

#	Process	A_{op} (%) (n : 1–2)	OE (%) (n : 1–2)	Throughput	Labor positions (Operator Supervision)	Yield elimination
	Ink mixing anode ^a	74.6	16.8–20.9	1 batch day ⁻¹	1 ½	—
	Ink mixing cathode ^a	74.6	45.2–56.4	1 batch day ⁻¹	1 ½	—
B	Coating (An and Ca) ^b	15.3–21.1	25.4–23.0	10 m min ⁻¹	2 ½	—
C	Transfer	30.7–42.2	12.5–11.4	10 m min ⁻¹	2 ½	Startup prints
D	CCM preparation	2.73–3.43	100	14 m min ⁻¹	1 ½	No
E	SG preparation	5.01–6.30	100	14 m min ⁻¹	1 ½	No
F	MEA _{5L} assembly	5.01–6.30	100	14 m min ⁻¹	1 ½	No
G	GDL preparation	9.59–12.1	87.2	8.8 m min ⁻¹	1 ½	—
H	GDL ₁ placement	7.53–9.46	100	9.3 m min ⁻¹	1 ½	GDL only
I	GDL ₂ placement and MEA _{7L} finalization	10.0–12.6	100	7.0 m min ⁻¹	1 ½	Yes

^aOE of the mixing processes are referenced to the used volume of the mixing unit.

^bOne coating line is shared for anode and cathode coating. Capital letters refer to the process shown in Figure 2.

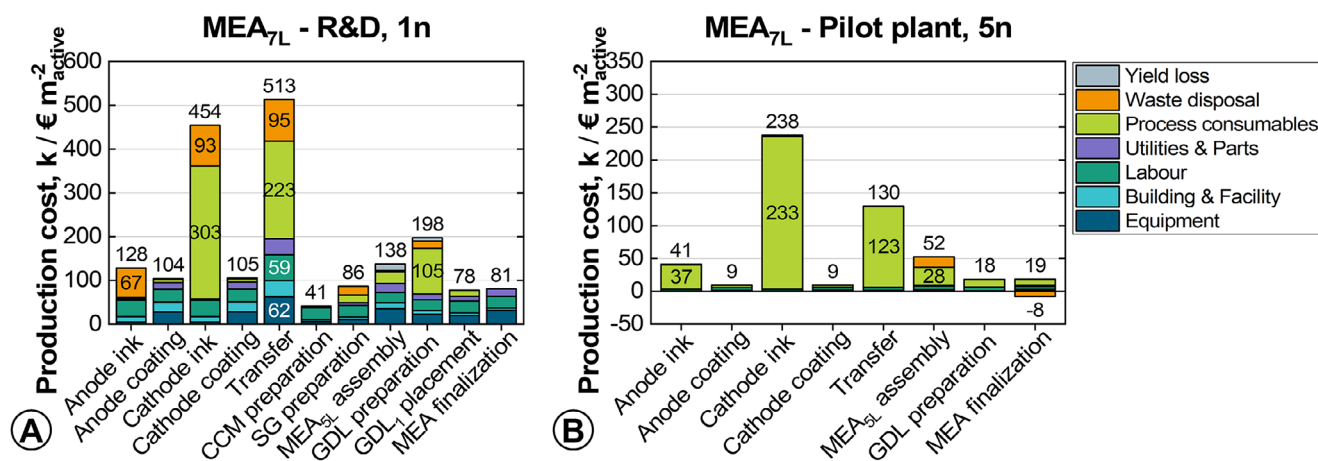


FIGURE 8 | Cost breakdown of a membrane electrode assembly (MEA_{7L}) production in the following scenarios. (A) “R&D, 1n” and (B) “Pilot Plant, 5n.”

Figure 8 shows the detailed cost distribution for the “R&D, 1n” and “Pilot plant, 5n” scenarios, revealing a different number of process steps between the two scenarios. This difference results from the adapted machinery setup. In the pilot plant scenarios, multiple steps of the CCM to MEA_{7L} conversion run in parallel, eliminating the need for separate processes. The “R&D, 1n” scenario exhibits higher waste shares due to the roll width mismatch with the Generic Stack design described in Section 2.3. In both scenarios, the main cost shares are distributed across the CCM production steps due to the materials they introduce. However, the cost composition changes significantly, while in the “R&D, 1n” scenario labor and equipment cost still play a significant role in each step, the “Pilot plant, 5n” scenario steps are dominated by consumable costs.

At the production level of the “Pilot Plant, 5n” scenario, further cost reductions through increased automation or parallel

production lines depend primarily on decreasing consumable prices rather than operational improvements. Ultimately, this is constrained by the raw material price of all specified MEA_{7L} components of 257€ m⁻² including a standard automotive supplier markup of 15%, as shown in Figure 7 [24]. Even at the lowest annual volume scenario, consumable costs are dominated by membrane and cathode catalyst expenses, mirroring the previously shown CCM cost structure (Figure 9A). This dominance intensifies at higher production volumes, where cathode catalyst and membrane contribute 73% to overall consumable costs (Figure 9B).

Comparing the results of this work with the “DOE Hydrogen Program Record 24004” of the Department of Energy (DOE), the 5000 systems per year scenario produces about the same annual area of MEA_{7L} as the “Pilot plant, 2n” scenario, resulting in 655€ m⁻² active for the MEA_{7L} components only [2]. The assump-

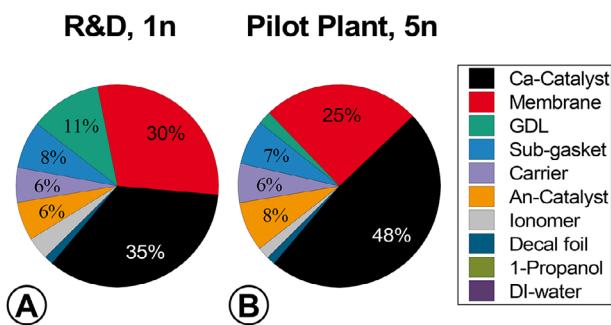


FIGURE 9 | Distribution of the consumable costs of different scenarios. (A) R&D scenario with a batch length of 250 m. (B) Pilot plant scenario with a batch length of 1250 m.

tions made can be found in Supporting Information S8. This result is significantly higher than the $547\text{€ m}^{-2}_{\text{active}}$ presented in this work, which can be attributed to differences in the modeling of the consumable costs as well as different assumptions regarding yields and tolerances.

Counterintuitively, the assumed yield losses and tolerances in this work result in a higher share of purchased materials in relation to the necessary materials for the active area. This is shown in Supporting Information S8 for the catalyst and membrane and shows a share of around 117% in this work compared to only 106% in the program record. On the other hand, this work assumes the partial recovery of discarded Pt, which lowers the total MEA_{7L} cost. Most significantly, the Pt price used in the DOE analysis is based on $\$_{2016}1500$ per troy oz, whereas this work uses a price of $\$_{2025}1364$ per troy oz, leading to a 29% reduction in Pt price when considering inflation. This difference accounts for the lower catalyst share and total MEA_{7L} cost compared to the program record. Consequently, a higher membrane share of total consumable costs compared to previous publications can be identified [2, 63]. This indicates that the membrane, in addition to the catalyst, should be emphasized in future cost improvements to the PEMFC through thickness reductions while maintaining electrochemical performance.

In summary, the analysis demonstrates that while focusing on technical boundaries, cost estimations comparable to the DOE can be achieved. Furthermore, economies of scale demonstrate the potential to decrease MEA_{7L} area costs by a factor of four in the evaluated scenarios. An alternative perspective can view the R&D scenario as representing a general low A_{op} due to variable causes. While a high A_{op} in the pilot plant scenarios mask machine investment costs through dominant consumable expenses, if the production or sales volumes are reduced, fixed costs regain significance in the overall cost structure.

3.4 | Sensitivity of the Pt-Loading

One way to reduce MEA_{7L} costs proposed in the literature is to reduce the platinum content [64]. However, when considering the cost per kW, any cost savings must be weighed against the resulting performance losses. Ideally, novel materials would facilitate platinum reduction while maintaining performance,

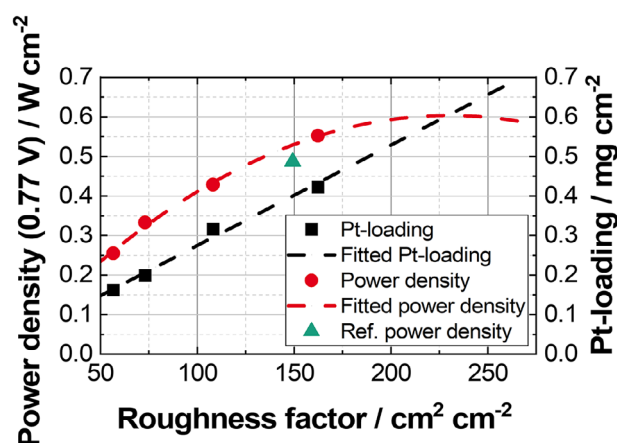


FIGURE 10 | Cell performance at different Pt-loadings at the cell voltage of 0.77 V. The reference performance datapoint is taken from Ney et al. [66].

but current materials face inherent limitations in achieving this goal [65].

To estimate the performance, single cell testing has been performed for cells with cathode Pt-loadings ranging from 0.17 to $0.42 \text{ mg}_{\text{Pt}} \text{ cm}^{-2}$. Since additional losses and changes in operating conditions are expected when transitioning to a full stack design, the single cell performance is proportionally scaled down to the reference performance observed in a measured stack [66]. The full polarization curves can be found in Figure S4. To align with the BOL assumption of the DOE, the performance is investigated at the operation point of 0.77 V [2].

The performance data in Figure 10 at 100% RH is given as function of the RF, since uncertainties in the Pt-loading measurements make curve fitting unreliable. The data exhibits a quadratic trend, consistent with previous literature findings, indicating that an increase of the RH and consequently the Pt-loading does not yield proportional performance improvements [65, 67–69]. This behavior is explained by increasing CL thicknesses, which consequently increases ohmic resistances in the layer [65]. Based on the observations in the literature, it is assumed, that the quadratic curve can be extrapolated to RFs and corresponding Pt-loadings outside the measured range. This results in a modeled maximum performance of 0.6 W cm^{-2} at a RF of $228 \text{ cm}^2 \text{ cm}^{-2}$, with an equivalent Pt-loading of $0.6 \text{ mg}_{\text{Pt}} \text{ cm}^{-2}$. The conversion between Pt-loading and RF is accomplished via the linearly fitted function shown in Figure 10. While these relationships are applied in this work, it should be noted that exact performance behavior is highly material- and operation-dependent. Performance evaluation at a single operation point fails to capture multiple design objectives required for the operation of fuel cells over a range of operating points.

Combining the performance information with the previously introduced cost model, shows that each scenario exhibits a minimal cost point. This is displayed in Figure 11 as cost per kW, where three input parameters are varied for the scenarios with the highest and lowest throughput. As reference, the Pt price and the capital expenditures for machinery (CAPEX) are varied in the same range as the Pt loading.

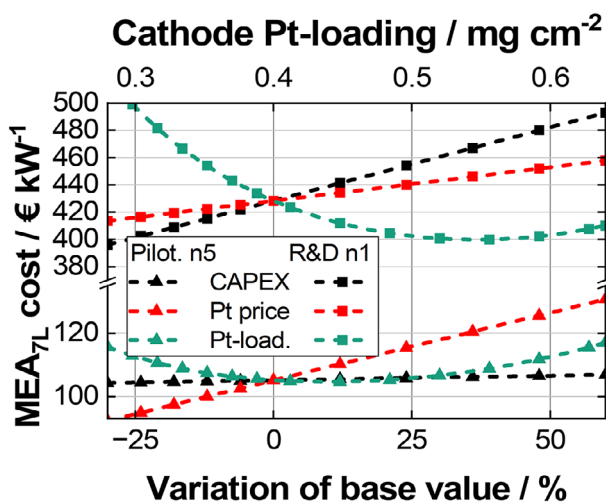


FIGURE 11 | MEA_{7L} cost per kW as a function of varying selected input parameters. Each line represents an independent variation of the indicated input parameter for the specified scenario. Variations in Pt-loading are coupled with the cell performance shown in Figure 10.

The first two input parameters demonstrate a linear relationship with the final MEA_{7L} cost. The relative gradients of these curves correspond to the relative cost share, previously illustrated in Figure 7. The steeper CAPEX gradient visually confirms its greater influence relative to Pt price in the “R&D, 1n” scenario, while this trend is reversed for the “Pilot plant, 5n” scenario. In contrast, the variation of the cathode Pt-loading shows a quadratic relationship consistent with the performance data. Lowering the Pt-loading from the original setpoint of 0.4 mg_{Pt} cm⁻² reduces the MEA_{7L} cost per m², but the reduced amount of Pt cannot offset the reduced performance, leading to an increase in cost per kW. The minimum cost per kW is determined to be at 0.44 mg_{Pt} cm⁻² for the “Pilot plant, 5n” scenario and 0.54 mg_{Pt} cm⁻² for the “R&D, 1n” scenario.

This demonstrates, that in both presented scenarios, it is advantageous to increase the Pt-loading rather than to decrease it. In addition, the effect of degradation was not considered in this analysis, which would require an additional increase of the Pt-loading to enable a longer cell lifetime [67]. This can be attributed to the fact that reducing the loading does not reduce all other costs necessary for the MEA_{7L} production. These can be considered fixed costs in this investigation which are not lowered when reducing the Pt-loading. Since the “R&D, 1n” scenario consists of a higher share of fixed costs, it is more advantageous to produce cells close to the performance maximum. On the other hand, when the dependance on fixed costs is lower relative to the variable Pt-loading, it can be advantageous to reduce the loading and produce cells below the theoretical performance maximum of the material combination, as shown for the “Pilot plant, 5n” scenario.

The presented findings are highly dependent on the selected materials as well as the operating point and represent examples, demonstrating the capability of connecting cost calculations with material research. Shifting the curve of optimal cost per performance toward lower Pt-loadings, thereby reducing the total MEA_{7L} costs is expected to be achieved with further material

and process developments. This integrated approach enables comprehensive evaluation of these novel materials and PEMFC design characteristics, providing a framework for optimizing the cost-performance relationship in fuel cell development.

4 | Conclusion

This study successfully applies the TCO framework, adapted for R2R manufacturing, to the fuel cell production while demonstrating comparable cost estimations for the MEA_{7L} as published by the DOE.

By focusing on technical manufacturing constraints, as given by the acquired machinery though the publicly funded project H2GO-R2MEA, the analysis enables detailed comparison of different manufacturing technologies and scenarios for the MEA_{7L} production. The discussed scenarios represent best-case conditions, focusing on technical feasibility rather than general pricing estimates.

The investigation confirms that economies of scale lead to significant cost reduction in MEA_{7L} production, reducing costs by 75% from 2086€ m⁻²_{active} in the lowest annual volume R&D scenario to 512€ m⁻²_{active} in the pilot plant scenario with the highest annual volume. This is accompanied by a transformation of the cost structure as the share of consumables increases from 48% of total expenses in the R&D scenario to 90% in the pilot plant scenario, with the cathode catalyst and membrane contributing 73% of consumable costs. This demonstrates the strong influence of material costs even at early stages of annual production, emphasizing the need for continued material innovations.

Combining the observed quadratic performance relationship as a function of the RF/Pt-loading with the introduced continuous process cost of ownership model reveals the existence of a cost per kW optimum. With the specific set of materials, optimal Pt-loadings above the conventional 0.4 mg_{Pt} cm⁻² were identified, depending on the production scenario. Scenarios with higher shares of Pt-independent costs shift the cost optimum closer to the performance optimum of the MEA_{7L}, while scenarios with lower shares allow for reduced optimal Pt-loadings.

Regarding manufacturing technologies, the comparison of different coating methods shows no significant cost impact, assuming identical levels of yield, production speed and MEA_{7L} performance. This indicates that the coating technology selection must consider factors beyond direct costs. Future work should focus on achieving the yields and process speeds assumed in this study, including process steps transforming the CCM to a MEA_{7L}. This should be complemented by evaluating different process pathways and investigating the impact of the coating technology on cell performance. The importance of achieving low yield losses is emphasized, as they create cascading effects that reduce the effective throughput throughout the production chain. This highlights the need for robust defect detection systems and mitigation strategies to prevent additional downstream costs after the MEA_{7L} production through early-stage detection. Successfully addressing these yield and detection challenges, combined with material cost innovations, represents the primary pathway for further fuel cell costs reductions.

Acknowledgments

The authors would like to thank Baljeet Singh Goraya and Dr.-Ing. Sebastian Nold for providing the SCost TCO model for further development and Patrick Schneider for conducting the cell testing and characterization. The authors also thank the machine and consumables manufacturers for their valuable input. In addition, the authors thank the Federal Ministry for Transport (BMV) and the National Organization Hydrogen and Fuel Cell Technology (NOW) for the financial support of the project H2GO-R2MEA (03B11027C) and the Project Agency Jülich (PTJ) for the administration as well as all for the good cooperation.

Open access funding enabled and organized by Projekt DEAL.

Conflicts of Interest

The authors declare no conflicts of interest.

Data Availability Statement

The data that support the findings of this study are available from the corresponding author upon reasonable request.

References

1. S. Rasmussen, *Springer Texts in Business and Economics* (Springer, 2013).
2. G. Kleen and W. Gibbons, *DOE Hydrogen Program Record 24004. Heavy-Duty Fuel Cell System Cost—2023* (2024).
3. M. Crippa, D. Guizzardi, M. Banja, et al., *CO₂ Emissions of All World Countries*, JRC/IEA/PBL 2022 Report, EUR 31182 (Publications Office of the European Union, 2022).
4. I. Staffell, D. Scamman, A. Velazquez Abad, et al., “The Role of Hydrogen and Fuel Cells in the Global Energy System,” *Energy & Environmental Science* 12 (2019): 463–491, <https://doi.org/10.1039/C8EE01157E>.
5. European Automobile Manufacturers’ Association (ACEA), Report—Vehicles in Use, Europe 2022, January 19, 2022, <https://www.acea.auto/publication/report-vehicles-in-use-europe-2022/>.
6. Addressing the Heavy-Duty Climate Problem, September 16, 2022, <https://www.transportenvironment.org/articles/addressing-the-heavy-duty-climate-problem>.
7. J. Wang, H. Wang, and Y. Fan, “Techno-Economic Challenges of Fuel Cell Commercialization,” *Engineering* 4 (2018): 352–360, <https://doi.org/10.1016/j.eng.2018.05.007>.
8. A. Kampker, P. Ayvaz, C. Schön, J. Karstedt, R. Förstmann, and F. Welker, “Challenges Towards Large-Scale Fuel Cell Production: Results of an Expert Assessment Study,” *International Journal of Hydrogen Energy* 45 (2020): 29288–29296, <https://doi.org/10.1016/j.ijhydene.2020.07.180>.
9. L. Ney, J. Hog, R. Singh, et al., “Challenges of Fabricating Catalyst Layers for PEM Fuel Cells Using Flatbed Screen Printing,” *Journal of Coatings Technology and Research* 20 (2023): 73–86, <https://doi.org/10.1007/s11998-022-00710-1>.
10. S. A. Mauger, K. C. Neyerlin, A. C. Yang-Neyerlin, K. L. More, and M. Ulsh, “Gravure Coating for Roll-to-Roll Manufacturing of Proton-Exchange-Membrane Fuel Cell Catalyst Layers,” *Journal of the Electrochemical Society* 165 (2018): F1012–F1018, <https://doi.org/10.1149/2.0091813jes>.
11. D. Mitra, K. Heinrich, S. Gierse, et al., “Direct Deposition of Catalyst Layers on Polymer Electrolyte Membrane (PEM) for Fuel Cells With Controlled Platinum Distribution by Inkjet Printing,” *Journal of Power Sources* 638 (2025): 236503, <https://doi.org/10.1016/j.jpowsour.2025.236503>.
12. M. Klingele, B. Britton, M. Breitwieser, et al., “A Completely Spray-Coated Membrane Electrode Assembly,” *Electrochemistry Communications* 70 (2016): 65–68, <https://doi.org/10.1016/j.elecom.2016.06.017>.
13. G. Pätzold, M. Maier, L. Löttert, A. T. S. Freiberg, S. Thiele, and D. Dworschak, “Graded Roll-to-Roll Slot Die Coating for High-Throughput Catalyst Layer Studies,” *ChemElectroChem* 12 (2025): e202400688, <https://doi.org/10.1002/celec.202400688>.
14. P. Santangelo, M. Cannio, and M. Romagnoli, “Review of Catalyst-Deposition Techniques for PEMFC Electrodes,” *Tecnica Italiana—Italian Journal of Engineering Science* 63 (2019): 65–72, <https://doi.org/10.18280/ti-ijes.630109>.
15. H. H. Heimes, M. M. Kehrer, S. Hagedorn, and J. Hausmann, *Produktion von Brennstoffzellenkomponenten; 2. Auflage, PEM der RWTH Aachen und VDMA Eigendruck* (2022).
16. B. James, J. Huya-Kouadio, C. Houchins, and M. Gomez, *Mass Production Cost Estimation of Direct H₂ PEM Fuel Cell Systems for Transportation Applications (2017–2021)*, Final Report DOE-SA–7600 (Strategic Analysis, 2021).
17. M. Wei, A. Mayyas, and T. Lipman, et al., “Fuel Cell Systems, Total Cost of Ownership,” *Springer Reference*, ed. R. A. Meyers (Springer, 2019), https://doi.org/10.1007/978-1-4939-2493-6_1020-1.
18. P. Marocco, D. Ferrero, A. Lanzini, and M. Santarelli, *Manufacturing Cost Analysis of PEM Fuel Cell Systems for 5- and 10-kW Backup Power Applications/DOE* (DOE, 2016).
19. M. Gebert, *Benchmarking-Methodik für Komponenten in Polymerelektrolyt-Brennstoffzellen, 2004* (Zugl.: Aachen, Techn. Hochsch., Diss., 2004).
20. A. Kampker, H. Heimes, M. Kehrer, S. Hagedorn, P. Reims, and O. Kaul, “Fuel Cell System Production Cost Modeling and Analysis,” *Energy Reports* 9 (2023): 248–255, <https://doi.org/10.1016/j.egy.2022.10.364>.
21. Semiconductor Equipment and Materials International (SEMI), *SEMI E35-0312: Guide to Calculate Cost of Ownership (COO) Metrics for Semiconductor Manufacturing Equipment* (Semiconductor Equipment and Materials International (SEMI), 2018), www.semi.org.
22. S. Nold, “Techno-ökonomische Bewertung neuer Produktionstechnologien entlang der Photovoltaik-Wertschöpfungskette. Modell zur Analyse der Total Cost of Ownership von Photovoltaik-Technologien” (diss., Fraunhofer Verlag, 2019).
23. F. Field, R. Kirchain, and R. Roth, “Process Cost Modeling: Strategic Engineering and Economic Evaluation of Materials Technologies,” *JOM Journal of the Minerals Metals and Materials Society* 59 (2007): 21–32, <https://doi.org/10.1007/s11837-007-0126-0>.
24. B. D. James, J. M. Huya-Kouadio, C. Houchins, et al., *Mass Production Cost Estimation of Direct H₂ PEM Fuel Cell Systems for Transportation Applications: 2018 Update* (2018).
25. VDMA, *Semiconductor Equipment and Materials International (SEMI)* (2014).
26. Semiconductor Equipment and Materials International (SEMI) SEMI E10-0814E: Specification for Definition and Measurement of Equipment Reliability, Availability, and Maintainability (RAM) (Semiconductor Equipment and Materials International (SEMI), 2014).
27. Semiconductor Equipment and Materials International (SEMI) SEMI E79-0814E: Specification for Definition and Measurement of Equipment Productivity (Semiconductor Equipment and Materials International (SEMI), 2014), www.semi.org.
28. S. H. Yeo, B. K. Ngoi, and H. Chen, “A Cost-Tolerance Model for Process Sequence Optimisation,” *International Journal of Advanced Manufacturing Technology* 12 (1996): 423–431, <https://doi.org/10.1007/BF01186931>.
29. L. F. Wong, *A Generalized Learning Curve Adapted for Purchasing and Cost Reduction Negotiations*, MHCS 122, 2900 Community College Avenue (Cuyahoga Community College, 2012).
30. M. A. Kromer, F. Joseck, T. Rhodes, M. Guernsey, and J. Marcinkoski, “Evaluation of a Platinum Leasing Program for Fuel Cell Vehicles,” *International Journal of Hydrogen Energy* 34 (2009): 8276–8288, <https://doi.org/10.1016/j.ijhydene.2009.06.052>.

31. T. Uekert, H. M. Wikoff, and A. Badgett, "Electrolyzer and Fuel Cell Recycling aor a Circular Hydrogen Economy," *Advanced Sustainable Systems* 8 (2023): 2300449, <https://doi.org/10.1002/adsu.202300449>.
32. Lohnnebenkosten in Deutschland in Euro, <https://www.destatis.de/DE/Themen/Arbeit/Arbeitskosten-Lohnnebenkosten/Tabellen/lohnkosten-deutschland.html>.
33. IG Metall-Tarifinfo: Zuschläge, <https://www.igmetall.de/tarif/tarif Tabellen/wie-hoch-sind-die-zuschlaege>.
34. Average Monthly Earnings of Employees by Sex and Occupation (2025), <https://ilostat.ilo.org/data/>.
35. Understanding the Cost of A Cleanroom (2020), <https://www.achengineering.com/cost-factors-clean-room/>.
36. H. Snellen and A. Tschöpel, *Cost of Capital Study 2024*. The New Dilemma: Balancing Interest Rates and Growth.
37. Harmonisierter Verbraucherpreisindex: Deutschland, Jahre (2025), <https://www-genesis.destatis.de/datenbank/online/statistic/61121/table/61121-0001>.
38. K. Frölich, "Der Decal-Prozess zur Herstellung katalysatorbeschichteter Membranen für PEM-Brennstoffzellen," PhD thesis, Karlsruher Institut für Technologie (KIT), (2015).
39. H. Liu, L. Ney, N. Zamel, and X. Li, "Effect of Catalyst Ink and Formation Process on the Multiscale Structure of Catalyst Layers in PEM Fuel Cells," *Applied Sciences* 12 (2022): 3776, <https://doi.org/10.3390/app12083776>.
40. D. Ye and Z. Zhan, "A Review on the Sealing Structures of Membrane Electrode Assembly of Proton Exchange Membrane Fuel Cells," *Journal of Power Sources* 231 (2013): 285–292, <https://doi.org/10.1016/j.jpowsour.2013.01.009>.
41. The ZSW HyFaB Generic Stack (2024), <https://www.zsw-bw.de/en/projects/brennstoffzellen/generic-fuel-cell-stack-open-development-platform-for-industry.html>.
42. L. Ney, N. Seidl, R. Singh, et al., "Screen Printing Catalyst Inks With Enhanced Process Stability for PEM Fuel Cell Production," *Fuel Cells* 25 (2025): 1615–6846, <https://doi.org/10.1002/fuce.202400158>.
43. P. Quarz, N. Zimmerer, L. Janning, A.-M. Steck, P. Scharfer, and W. Schabel, "Ink Processing and its Influence on Particle Size Distribution, Ionomer Requirements and Electrode Properties in Polymer Electrolyte Membrane Fuel Cell and Electrolyzer Catalyst Coated Membranes," *Energy Technology* 14 (2025): e202501844, <https://doi.org/10.1002/ente.202501844>.
44. A. S. Amin, et al., "The Impact of Ink Processing on Key Characteristics of Platinum Detachment and Pore Structure to Optimize Fuel Cell Performance," *International Journal of Hydrogen Energy* 144 (2025), <https://doi.org/10.1016/j.ijhydene.2025.04.450>.
45. S. A. Mauger, M. Wang, F. C. Cetinbas, et al., "Development of High-Performance Roll-to-Roll-Coated Gas-Diffusion-Electrode-Based Fuel Cells," *Journal of Power Sources* 506 (2021): 230039, <https://doi.org/10.1016/j.jpowsour.2021.230039>.
46. M. Stähler, A. Stähler, F. Scheepers, M. Carmo, and D. Stolten, "A Completely Slot Die Coated Membrane Electrode Assembly," *International Journal of Hydrogen Energy* 44 (2019): 7053–7058, <https://doi.org/10.1016/j.ijhydene.2019.02.016>.
47. J. Sharma, X. Lyu, T. Reshetenko, et al., "Catalyst Layer Formulations for Slot-Die Coating of PEM Fuel Cell Electrodes," *International Journal of Hydrogen Energy* 47 (2022): 35838–35850, <https://doi.org/10.1016/j.ijhydene.2022.08.157>.
48. R. Diehm, H. Weinmann, J. Kumberg, et al., "Edge Formation in High-Speed Intermittent Slot-Die Coating of Disruptively Stacked Thick Battery Electrodes," *Energy Technology* 8 (2020): 1900137, <https://doi.org/10.1002/ente.201900137>.
49. S. Spiegel, T. Heckmann, A. Altvater, R. Diehm, P. Scharfer, and W. Schabel, "Investigation of Edge Formation During the Coating Process of Li-Ion Battery Electrodes," *Journal of Coatings Technology and Research* 19 (2022): 121–130, <https://doi.org/10.1007/s11998-021-00521-w>.
50. P. Quarz, N. Zimmerer, P. Scharfer, and W. Schabel, "About Drying Phenomena of Fuel Cell and Electrolyzer CCM Inks: Selectivity of the Evaporation of 1-Propanol/Water Mixtures," *Fuel Cells* 24 (2024): 108–121, <https://doi.org/10.1002/fuce.202300252>.
51. S. Jaiser, M. Müller, M. Baunach, W. Bauer, P. Scharfer, and W. Schabel, "Investigation of Film Solidification and Binder Migration During Drying of Li-Ion Battery Anodes," *Journal of Power Sources* 318 (2016): 210–219, <https://doi.org/10.1016/j.jpowsour.2016.04.018>.
52. S. Jaiser, J. Kumberg, J. Klaver, et al., "Microstructure Formation of Lithium-Ion Battery Electrodes During Drying—An Ex-situ Study Using Cryogenic Broad Ion Beam Slope-Cutting and Scanning Electron Microscopy (Cryo-BIB-SEM)," *Journal of Power Sources* 345 (2017): 97–107, <https://doi.org/10.1016/j.jpowsour.2017.01.117>.
53. L. Ney, J.-L. Wolken, R. Singh, et al., "Impact of the Drying Temperature During Catalyst Layer Manufacturing on PEM Fuel Cell Performance," *Meeting Abstract MA2022-01* (2022): 1422, <https://doi.org/10.1149/MA2022-01351422mtgabs>.
54. L. Ney, N. Göttlicher, R. Lohmann, et al., "Rotary Screen Printing of Catalyst Layers for Polymer Electrolyte Membrane Fuel Cells," *International Journal of Hydrogen Energy* 202 (2026): 153053, <https://doi.org/10.1016/j.ijhydene.2025.153053>.
55. P. Schneider, A.-C. Scherzer, L. Ney, et al., "In-Situ Characterization of Cathode Catalyst Degradation in PEM Fuel Cells," *Scientific Data* 11 (2024): 828, <https://doi.org/10.1038/s41597-024-03662-w>.
56. S. Seabold and J. Perktold, "Statsmodels: Econometric and Statistical Modeling with Python," 9th Python in Science Conference, (2010): 92–96, <https://doi.org/10.25080/Majora-92bfi922-011>.
57. F. Pedregosa, G. Varoquaux, A. Gramfort, et al., "Scikit-Learn: Machine Learning in Python," *Journal of Machine Learning Research* 12 (2011): 2825–2830.
58. PGM Prices and Trading (2025), <https://matthey.com/products-and-markets/pgms-and-circularity/pgm-management/>.
59. B. James, J. Huya-Kouadio, C. Houchins, M. J. Jensen, and K. R. McNamara, *DRAFT: Mass Production Cost Estimation of Direct H₂ PEM Fuel Cell Systems for Transportation Applications: 2023 Update on Heavy-Duty and Medium-Duty Vehicles* (2023).
60. C. Daniel and S. Mauger in *Hydrogen and Fuel Cells Program Annual Merit Review* (2019).
61. W. Bernhart, S. Riederle, M. Yoon, and W. G. Aulbur, "Fuel Cells—A Realistic Alternative for Zero Emission?," *Auto Tech Review* 3 (2014): 18–23, <https://doi.org/10.1365/s40112-014-0568-z>.
62. H. H. Heimes, A. Kampker, S. Wennemar, P. Lorenz, and G. Bockey, *Production Process of a Lithium-Ion Battery Cell, PEM der RWTH Aachen und VDMA Eigendruck* (2023).
63. E. J. Carlson, P. Kopf, J. Sinha, S. Sriramulu, and Y. Yang, *Cost Analysis of PEM Fuel Cell Systems for Transportation: September 30, 2005* (2005).
64. N. Zamel, "The Catalyst Layer and its Dimensionality—A Look Into its Ingredients and How to Characterize Their Effects," *Journal of Power Sources* 309 (2016): 141–159, <https://doi.org/10.1016/j.jpowsour.2016.01.091>.
65. P. Schneider, M. Batool, A. O. Godoy, et al., "Impact of Platinum Loading and Layer Thickness on Cathode Catalyst Degradation in PEM Fuel Cells," *Journal of the Electrochemical Society* 170 (2023): 024506, <https://doi.org/10.1149/1945-7111/acb8df>.
66. L. Ney, D. Herbst, N. Wengenmeyr, et al., "From Catalyst Ink to PEM Fuel Cell Stack: First Full-Size Screen Printed Catalyst Layers Tested Within a Generic Stack," *ECS Transactions* 114 (2024): 329–337, <https://doi.org/10.1149/11405.0329ecst>.
67. P. Gazdzicki, J. Mitzel, A. M. Dreizler, M. Schulze, and K. A. Friedrich, "Impact of Platinum Loading on Performance and Degradation

of Polymer Electrolyte Fuel Cell Electrodes Studied in a Rainbow Stack,” *Fuel Cells* 18 (2018): 270–278, <https://doi.org/10.1002/fuce.201700099>.

68. L. Hao, K. Moriyama, W. Gu, and C.-Y. Wang, “Modeling and Experimental Validation of Pt Loading and Electrode Composition Effects in PEM Fuel Cells,” *Journal of the Electrochemical Society* 162 (2015): F854–F867, <https://doi.org/10.1149/2.0221508jes>.

69. H. A. Gasteiger, J. E. Panels, and S. G. Yan, “Dependence of PEM Fuel Cell Performance on Catalyst Loading,” *Journal of Power Sources* 127 (2004): 162–171, <https://doi.org/10.1016/j.jpowsour.2003.09.013>.

70. B.-S. Kwon, K.-H. Lee, and A. Jang, “The Estimation of Total Cost Through the Financial Assessment of Customized High Purity Industrial Water,” *Journal of Korean Society of Environmental Engineers* 40 (2018): 428–437, <https://doi.org/10.4491/KSEE.2018.40.11.428>.

71. Trend Indexes—businessanalytiq (2024), <https://businessanalytiq.com/index/>.

72. Cerium Oxide Price Globally 2009–2030 (2025), <https://www.statista.com/statistics/450146/global-reo-cerium-oxide-price-forecast/>.

73. PEN—Rod (2025), <https://www.goodfellow.com/de/pen-rod-group>.

Supporting Information

Additional supporting information can be found online in the Supporting Information section.

Supporting File: fuce70058-sup-0001-SuppMat.docx.